# Propulsion System Modeling for Small Fixed-Wing UAVs

Erlend M. Coates, Andreas Wenz, Kristoffer Gryte, Tor Arne Johansen

***Abstract*—This paper presents a model of an electrical propulsion system typically used for small fixed wing unmanned aerial vehicles (UAVs). Such systems consist of a power source, an electronic speed controller and a brushless DC motor which drives a propeller. The electrical, mechanical and aerodynamic subsystems are modeled separately and then combined into one system model, aiming at bridging the gap between the more complex models used in manned aviation and the simpler models typically used for UAVs. Such a model allows not only the prediction of thrust but also of the propeller speed and consumed current. This enables applications such as accurate range and endurance estimation, UAV simulation and model-based control, in-flight aerodynamic drag estimation and propeller icing detection. Wind tunnel experiments are carried out to validate the model, which is also compared to two UAV propulsion models found in the literature. The experimental results show that the model is able to predict thrust well, with a root mean square error (RMSE) of 2.20 percent of max thrust when RPM measurements are available, and an RMSE of 4.52 percent without.**

## I. Introduction

In recent years, the use of electrically propelled small unmanned aerial vehicles (UAVs) has been expanding into a wide range of possible use cases, like mapping, surveillance, as well as search and rescue missions. These applications have been made possible by an increased range of these UAV platforms, which is enabled by advances in battery technology, increased autonomy of autopilot systems and the use of efficient electrical propulsion systems. It is necessary to design and identify models of these propulsion systems to use them to their maximal potential and enable safe autonomous flight.

An accurate model allows the identification of faults on both the motor and the propeller, which might be caused by short circuits, propeller icing or increases in friction due to ball bearing faults. In addition, such a model allows a more accurate prediction of the power consumption, improving the accuracy of range and endurance predictions. Also when simulating UAV flights, a propulsion model is necessary to achieve a high fidelity simulation environment. Finally, the model can also be used in the design of model-based controllers and observers.

E. M. Coates, A. Wenz, K. Gryte and T. A. Johansen are with the Centre of Autonomous Marine Operations and Systems (NTNU AMOS), Department of Engineering Cybernetics, at the Norwegian University of Science and Technology, Trondheim, Norway

Corresponding Author: erlend.m.l.coates@ntnu.no

An electrical propulsion system typically consists of an electrical motor, in most cases a synchronous motor, which is controlled by an electronic speed controller (ESC). The ESC converts the direct current provided by the battery into a pulse width modulated alternating current. Because of their similar behavior to traditional brushed direct current (DC) motors, the combination of an ESC and the synchronous drive is often referred to as a brushless dc motor (BLDC motor). The choice of BLDC motors for small UAVs is popular due to their compact size, better power-to-weight ratio and low noise characteristics in comparison to the aforementioned brushed DC motors. Attached to the shaft of the BLDC motor is a propeller which converts the rotational velocity and torque into a thrust force.

The modeling of such a propulsion system is challenging, since it requires knowledge of the electrical, mechanical and aerodynamic subsystems. Approaches for UAV propulsion modeling have been focused on finding simple models which do not discriminate between electrical and combustion engine propulsion. In [3] a very simple model is proposed based on momentum/actuator disk theory [14], furthermore a linear throttle to angular velocity relationship and constant propulsion efficiency are assumed. [12] uses polynomial models in order to predict propeller speed and thrust for a fixed-wing UAV. A detailed model of a UAV thruster is presented in [11], using blade element momentum theory (BEMT), but relies on extensive amounts of propeller data in order to identify the required coefficients and only validation with static tests is presented. The aforementioned models are valid for cruise flight only. Additional propeller effects for simulation of agile/aerobatic maneuvers, such as propeller slipstream effects, are discussed in [20].

There exists a variety of BLDC motor models. In [15] the three-phase model is reduced to an equivalent single phase model and used for fault detection. This model is extended with a more detailed description of possible losses in [10].

In order to calculate the thrust created by a propeller, momentum theory was proposed in the 19th century by Rankine [18] and extended by Froude [9]. Betz [5] further extended that by taking propeller drag into account. He explains that even under ideal conditions the propeller efficiency is bounded, limiting the portion of the power that can be induced on, or extracted from, the prevailing wind. A detailed treatment of propeller models for different purposes is given in [14].

Although modeling of propulsion systems for manned aircraft is well researched, the results are not always applicable to small low cost UAVs. The required propeller and motor data are often not available from the manufacturer and detailed parameter identification would be cost prohibitive for the platforms considered. Small UAVs are most often electrically propelled, which in comparison with propulsion systems based on internal combustion engines, can easily measure the input power as well as the angular velocity of the rotor. Simple models applicable for small UAVs are presented in [2] and [3]. However, these models seem to lack any published experimental validation with wind tunnel data making it difficult to judge their accuracy.

This paper proposes a physical model of the propulsion system of an electrically propelled UAV, aiming to bridge the gap between the complex propulsion models published for larger manned aircraft and the simpler models found in the UAV literature. Based on measurements of the battery voltage, throttle and airspeed, this model allows prediction not only of the thrust force, but also of the battery current and the propeller speed. The model will be validated using wind tunnel data obtained from a typical propulsion system found on small fixed-wing UAVs. The accuracy of the model is then compared to the accuracy of the two modeling approaches found in [2] and [3]. Instead of including a model of the power source (e.g. the battery) in the model, we choose to use the supplied voltage and the commanded throttle as an input. This makes the model independent of the type of power source, allowing it to be used for both hybrid-electric propulsion systems, as well as battery powered propulsion, regardless of the state of charge and load on the battery.

## II. Physical Model

The propulsion system consists of several components which have electrical, mechanical and aerodynamic characteristics. In the following, we will model the electrical, mechanical and aerodynamic subsystems, then combine these models into one multiphysical model and formulate the identification problem. The modeling of the mechanical and electrical systems mainly follows [15], while the aerodynamic modeling is based on [14].

### A. Electrical System

The BLDC motor consists of an inverter stage, which transforms the DC current and voltage received from the battery to a three-phase alternating current (AC) signal. The AC signal is needed in order to create rotating magnetic fields in the stator, causing the permanent magnet rotor to rotate. A circuit diagram of the BLDC motor with inverter can be seen in Figure 1.

One coil can be modeled as:

$$u_1(t) - u_n = R_1 i_1(t) + \frac{d}{dt} L_1 i_1(t) + u_{E,1} \tag{1}$$

where $u_1$ and $u_n$ are the input voltage and neutral point voltage defined in Figure 1, $R_1$ is the combined coil and inverter resistance, $L_1$ is the coil inductance, $i_1$ is the current and $u_{E,1}$ is the back electromagnetic force (back-emf). The back-emf is given by

$$u_{E,1} = k_{E,1}\omega \tag{2}$$

where $\omega$ is the angular velocity of the rotor and $k_{E,1}$ is the back-emf constant.

The inverter stage consists of three bridges, each consisting of two switches which are typically realized as an anti-parallel insulated-gate bipolar transistor (IGBT) and diode. Within the ESCs regarded in this work, the inverters are triggered in order to produce a square wave modulation with a phase shift of $120°$ between each phase. This modulation scheme is often used in low cost ESC because it does not require a measurement of the rotor position via a hall sensor since the phase triggering can be done based on the back-emf [17].

Since square wave modulation is used, at each time instance two phases are conducting while one phase is open. Following [15], the circuit diagram can be simplified to the diagram shown in Figure 2, with $R = \frac{2}{3}(R_1 + R_2 + R_3)$, $L = \frac{2}{3}(L_1 + L_2 + L_3)$ and $k_E = \frac{2}{3}(k_{E,1} + k_{E,2} + k_{E,3})$

In the following modeling process, only the static case $\left(\frac{d}{dt} i_1(t) = 0\right)$ will be considered, which is typical for cruise flight. In addition, we will treat the coil inductance $L$ as an ideal integrator such that:

$$\int U_{dd}\delta_{pwm}(t)dt = U_{dd}\delta_t \tag{3}$$

where $U_{dd}$ is the battery voltage and $\delta_{pwm}(t) \in \{0, 1\}$. The throttle is defined as the duty cycle ratio

$$\delta_t = \frac{T_{on}}{T_p} \tag{4}$$

where $T_{on}$ is the time within a period $T_p$ in which the PWM signal is high. The voltage balance of this simplified circuit is then given by:

$$U_{dd}\delta_t = RI_a + k_E\omega \tag{5}$$

where $I_a$ is the average phase current. Rearranging yields the following expression for the average phase current:

$$I_a = \frac{U_{dd}\delta_t - k_E\omega}{R} \tag{6}$$

### B. Mechanical System

Assuming the motor torque constant equals the back-emf constant, the torque balance at the motor's shaft is given by:

$$\Theta\dot{\omega} = k_E(I_a - I_0) - c_v\omega - Q \tag{7}$$

where $I_0$ is the zero-load current, $c_v$ is the viscous friction coefficient, $\Theta$ is the moment of inertia of the rotor including the propeller and $Q$ is the aerodynamic torque created by propeller drag. Considering the static case, i.e. $\dot{\omega} = 0$, (7) can be rewritten to

$$k_E I_a = k_E I_0 + c_v\omega + Q \tag{8}$$

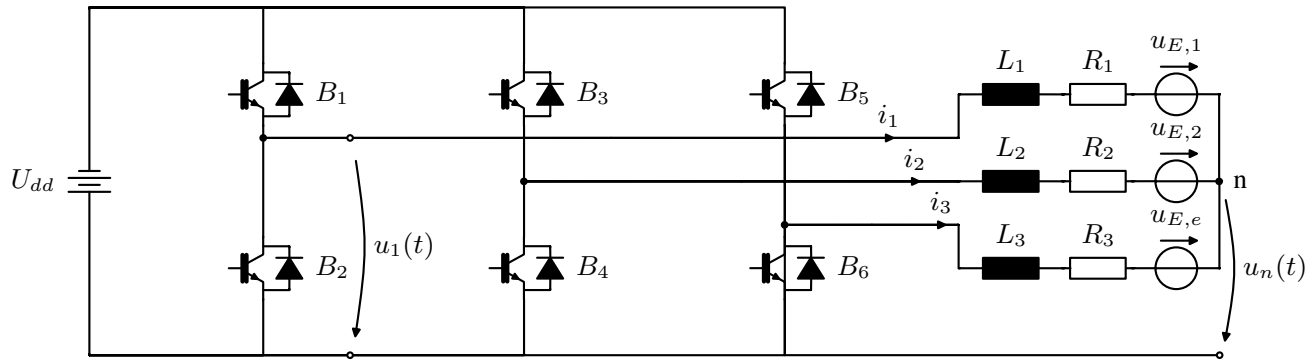


Fig. 1. Three phase circuit diagram of a BLDC motor.

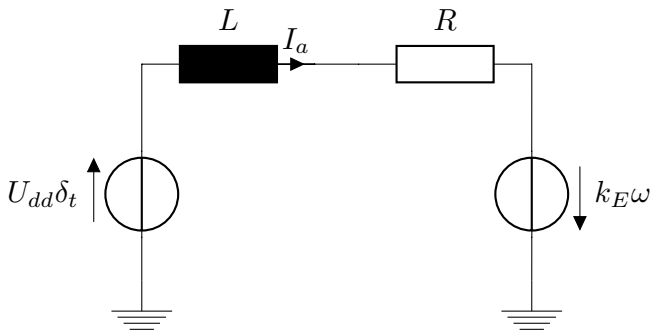


Fig. 2. Simplified Circuit diagram of a BLDC motor.

### C. Propeller Aerodynamics

When dealing with experimental propeller aerodynamics, the thrust, $T$, and torque, $Q$, are usually nondimensionalized by defining the thrust coefficient, $C_T$, and torque coefficient, $C_Q$ [14]:

$$C_T = \frac{4\pi^2 T}{\rho D^4 \omega^2} \tag{9}$$

$$C_Q = \frac{4\pi^2 Q}{\rho D^5 \omega^2} \tag{10}$$

where $\rho$ is the air density, and $D$ is the propeller diameter. The propeller speed, which equals the rotor angular velocity, is given by $\omega$.

$C_T$ and $C_Q$ are normally given as lookup tables. Neglecting Reynolds number effects, and Mach number effects, which occur at high rotation speeds, the thrust and torque coefficients mainly depends on the advance ratio $J = \frac{2\pi V_a}{\omega D}$ where $V_a$ is the airspeed. Polynomial parametrizations can be used [4]. In this work we use the following first order approximations:

$$C_T(J) = C_{T,0} + C_{T,1} J \tag{11}$$

$$C_Q(J) = C_{Q,0} + C_{Q,1} J \tag{12}$$

The thrust and torque is then given by:

$$T = \frac{\rho D^4}{4\pi^2} \left( C_{T,0} + C_{T,1} J \right) \omega^2 \tag{13}$$

$$Q = \frac{\rho D^5}{4\pi^2} \left( C_{Q,0} + C_{Q,1} J \right) \omega^2 \tag{14}$$

### D. Parameter Identification

Combining the electrical, mechanical and aerodynamic subsystems, one system model of the whole propulsion system is obtained. Parameter identification is carried out in three stages. Each parameter identification stage will be formulated as a separate nonlinear least squares problem.[1]

**Definition II.1.** Nonlinear Least Squares problem: Given a set of $m$ data points $(\boldsymbol{x}_i, y_i)$, $i = 1 \dots m$, and some nonlinear function $f(\boldsymbol{x})$ parameterized by a parameter vector $\boldsymbol{\theta}$, the nonlinear least squares problem is to minimize the criterion

$$J(\boldsymbol{\theta}) = \sum_{i=1}^{m} \left( y_i - f(\boldsymbol{x}_i, \boldsymbol{\theta}) \right)^2 \tag{15}$$

A solution $\boldsymbol{\theta}^*$ to (15) is given by

$$\boldsymbol{\theta}^* = \arg\min_{\boldsymbol{\theta}} J(\boldsymbol{\theta}) \tag{16}$$

This can be efficiently solved using the nonlinear least square solver provided by MATLAB which uses a trust-region-reflective algorithm as described in [7] and [6].

Measured variables in the experiment are the current $I_a$, the battery voltage $U_{dd}$, the throttle $\delta_t$, the propeller speed $\omega$ and the thrust force $T$. Except for the thrust, all these measurements are typically available in flight.

The three identification stages will now be properly set up in a form compatible with (15).

*1) Voltage Balance:* In order to identify the parameters $k_E$ and $R$, the voltage balance (5) is used. Defining $y_1 = U_{dd}\delta_t$, $x_{11} = \omega$, $x_{12} = I_a$, $\theta_{11} = k_E$ and $\theta_{12} = R$, (5) can be written

$$y_1 = \theta_{11} x_{11} + \theta_{12} x_{12} \triangleq f_1(\boldsymbol{x}_1, \boldsymbol{\theta}_1) \tag{17}$$

*2) Torque Balance:* Inserting Equations (6) and (14) into the torque balance given by (8) yields:

$$k_E I_0 + \omega \left( \frac{k_E^2}{R} + c_v \right) + \frac{\rho D^5}{4\pi^2} \left( C_{Q,0} + C_{Q,1} J \right) \omega^2 = U_{dd} \delta_t \frac{k_E}{R} \tag{18}$$

[1]It should be noted that although some problems are linear, the same method is used throughout the paper for consistency.

By using the solution for $k_E$ and $R$ from the previous stage, let us define $y_2 = \frac{k_E}{R} U_{dd} \delta_t$. By further defining $x_{21} = \omega$, $x_{22} = J$, $\theta_{21} = \frac{\rho D^5}{4\pi^2} C_{Q,1}$, $\theta_{22} = \frac{\rho D^5}{4\pi^2} C_{Q,0}$, $\theta_{23} = k_E^2/R + c_v$ and $\theta_{24} = k_E I_0$, (18) can be written

$$y_2 = (\theta_{21} x_{22} + \theta_{22}) x_{21}^2 + \theta_{23} x_{21} + \theta_{24} \triangleq f_2(\boldsymbol{x}_2, \boldsymbol{\theta}_2) \quad (19)$$

By solving for $\theta_{2j}, j = 1 \dots 4$, the torque coefficients $C_{Q,0}$, $C_{Q,1}$ as well as the zero-load current $I_0$ and the viscous friction coefficient $c_v$ can be calculated.

*3) Propeller Thrust:* Finally, the thrust coefficients $C_{T,0}$ and $C_{T,1}$ will be identified. Let $y_3 = C_T$. Then, from (9), we get

$$y_3 = \frac{4\pi^2 T}{\rho D^4 \omega^2} \quad (20)$$

By further defining $x_{31} = J$, $\theta_{31} = C_{T,0}$ and $\theta_{32} = C_{T,1}$, Equation (11) can be written

$$y_3 = \theta_{31} + \theta_{32} x_{31} \triangleq f_3(\boldsymbol{x}_3, \boldsymbol{\theta}_3) \quad (21)$$

## III. Approximate Models

With the goal of creating simple models that can be used for UAV simulation and autopilot design, several approximate models have been proposed in the literature. In this paper we will discuss two such models. We will refer to them as the *Beard & McLain model* [3] and the *Fitzpatrick model* [8], [2], respectively. These models have been used for simulation purposes, e.g. in [13], but, to the best of the authors' knowledge, no experimental validation of these models seem to be published. Therefore, in this work, these models will be fitted to wind-tunnel test data and compared to the physical model presented above.

As for the physical model we identify the needed parameters using the nonlinear least squares formulation.

### A. Beard & McLain Model

The *Beard & McLain model* is derived from a simple actuator disk model. It assumes a linear throttle to exit velocity relationship and a constant propeller efficiency. The propeller thrust is given by [3]:

$$T = 0.5 \rho S_p \eta_p ((k_m \delta_t)^2 - V_a^2) \quad (22)$$

where $S_p$ is the area swept out by the propeller disk, $\eta_p$ is an efficiency factor, and $k_m$ is a motor constant. The term $k_m \delta_t$ is the exit speed $V_e$, the speed of the air as it leaves the propeller.

### B. Fitzpatrick Model

In the *Fitzpatrick model*, the exit speed is assumed to be a function of throttle and airspeed given by:

$$V_e = V_a + \delta_t (k_m - V_a) \quad (23)$$

Applying momentum theory (see Equation (6.3) in [14]), this yields:

$$T = \rho S_p \eta_p (V_a + \delta_t (k_m - V_a)) \delta_t (k_m - V_a) \quad (24)$$

In the following, the two models will be evaluated and compared to the physical model by first identifying the needed coefficients from wind tunnel data and then evaluating their thrust prediction performance.

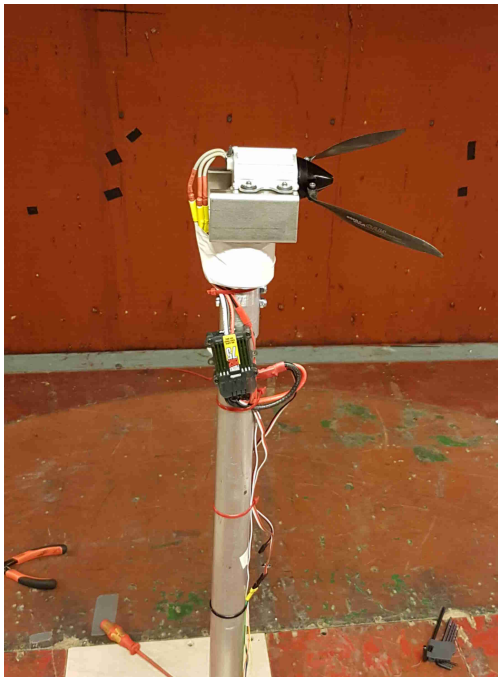

Fig. 3. Wind tunnel setup.

## IV. Experimental Setup

To collect data for parameter identification, and for validation and comparison of the models, a series of experiments were performed at the closed-circuit wind tunnel at the Department of Energy and Process Engineering at the Norwegian University of Science and Technology. The closed test section is 1.8 m high, 2.7 m wide and 11 m long and can produce freestream velocities up to 24 m/s. The tested hardware, which is used with the Skywalker X8 flying wing at NTNU's UAV-Lab, is listed in Table I.

The following section describe the sensors, hardware and software used for data acquisition. The process of experiment design and pre-processing of measured sensor data is then explained.

### A. Data Acquisition

The wind tunnel is equipped with

- a Schenck six-component force balance, for which one axis was used to measure the thrust and drag forces.
- a type-K thermocouple temperature sensor, to enable compensation for temperature-related fluid properties.
- a 10 Torr pressure transducer
- a controller for adjusting the angular velocity of the wind tunnel fan

The control and data acquisition of the wind tunnel is running on a National Instrument compactDAQ system, which is interfaced through a LabView graphical user interface. In addition to the wind tunnel and its sensors, the experimental setup consists of

- a back-EMF-based RPM sensor, Hobbywing HW-BQ2017
- a Mauch PL 100 hall-effect-based current and voltage sensor

TABLE I
HARDWARE OVERVIEW

| Propeller | Motor | ESC | Battery |
|---|---|---|---|
| Aeronaut CamCarbon 14x8" (foldable) | Hacker Motor A40-12S V2 14-pin KV610 | Jeti SPIN Pro 66 | Zippy Compact 5000mAh 4S 25C LiPo |

The above sensors were chosen because they are fairly accurate, and at the same time can easily be integrated in the standard payload of a UAV, since the open source autopilot ArduPilot can interface both sensors, thus enabling future online thrust estimates.

To synchronize the data from the wind tunnel with the RPM, current and voltage readings, the DUNE Unified Navigation Environment [16] was used.[2] The RPM and power sensors were connected to a PixHawk autopilot, running ArduPilot, and are incorporated into DUNE through the Mavlink protocol. The force, temperature and airspeed measurements from the wind tunnel was sent from LabView to DUNE over UDP.

The setup also consists of a motor interface, in which a series of PWM values that should be sent to the motor can be set, along with a time for how long each value should be held.

The motor, propeller, ESC and RPM sensor is mounted to a rod, to center it in the test section, which again is screwed onto the mass balance, as seen in Figure 3. For safety, the power supply and emergency switch was mounted by the operator desk outside the wind tunnel, along with the power module, Pixhawk autopilot, and computers running DUNE and LabView.

### B. Experiment Design

*a) Mass-balance calibration:* With the wind tunnel powered off, the force produced by a set of known calibration masses was measured, producing a linear mapping from mass-balance voltage to force.

*b) Zero-force calibration:* With the wind tunnel powered off, the force produced by the mass of the motor/propeller and the rest of the setup is measured. This reading will be subtracted from the subsequent measurements.

*c) Zero-thrust calibration:* With the wind tunnel spinning at the desired speed, but the motor turned off, the aerodynamic drag force produced by the motor/propeller and the rest of the setup is measured. This reading will be subtracted from the subsequent measurements, to isolate the thrust from the drag.

*d) Data collection:* For each desired airspeed, including zero, the motor was stepped through a series of PWM values from 1000-2000, with increments of 100. Each value was held for 5 seconds.[3]

[2]This is the framework we run in our UAVs, and the choice was purely from a practical perspctive: we already had interfaces to the RPM and power sensors, and had good familiarity with the framework.

[3]Please note that the setpoints of the wind tunnel was in angular velocity of its fan, not airspeed, as the mapping from angular velocity to airspeed varies with the temperature and static pressure of the air.

### C. Data Pre-Processing

Before fitting experimental data to the models developed in Sections II and III, some pre-processing of the data is needed.

*a) RPM Measurements:* The RPM sensor measures electrical RPM. The electrical RPM $n_e$ is related to the mechanical RPM $n$ through [1]:

$$n = n_e \frac{2}{N_p} \tag{25}$$

where $N_p$ is the number of rotor poles of the synchronous motor. $N_p = 14$ for the tested motor. The propeller speed in rad/s is then given by

$$\omega = \frac{2\pi}{60} n \tag{26}$$

*b) Computing Airspeed:* Given temperature measurements $T$, as well as measurements of static pressure $p_s$ and total (stagnation) pressure $p_t$, the airspeed can be computed. From Bernoulli's equation, the dynamic pressure $\bar{q}$ is given by [21]:

$$\bar{q} = \frac{1}{2}\rho V_a^2 = p_t - p_s \tag{27}$$

Solving this for $V_a$ yields

$$V_a = \sqrt{\frac{2\bar{q}}{\rho}} \tag{28}$$

The density $\rho$ changes with temperature and static pressure, and can be calculated using the ideal gas law [21]:

$$\rho = \frac{p_s}{R_{air} T} \tag{29}$$

where $R_{air}$ is the *specific gas constant* of air.

*c) Resampling:* Previous neighbor interpolation is used to get all sensor readings on the same frequency, 10 Hz, which was the highest common frequency of the sensors.

*d) Remove Dynamic Data:* Remove transients, as well as a time delay that is present between throttle changes and the RPM response. Figure 5 shows a zoomed in view where the dynamic parts of the data is removed.

*e) Miscellaneous:* To make the advance ratio well defined, data points with very small RPM values are removed. At higher airspeeds, the propeller is *windmilling*, i.e. spinning simply due to the wind at zero throttle settings. Because of this, data points at very low throttle, current and thrust were removed before curve fitting. Figure 4 shows how the windmilling parts of the data is removed from the dataset.

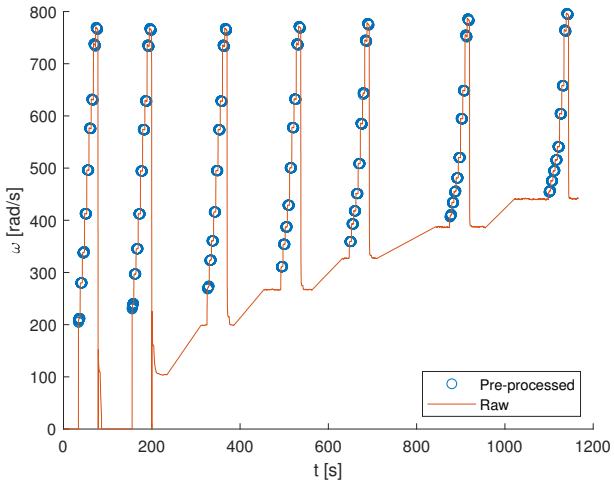


Fig. 4. Illustration of pre-processing.

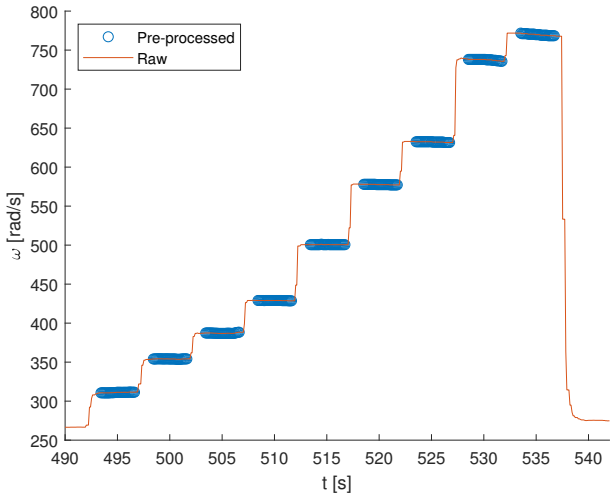


Fig. 5. Illustration of pre-processing, zoomed in view.

## V. Results and Discussion

### A. Voltage and Torque Balance Fits

Experimental trials shows that the voltage balance model (5) is more accurate in high load than in low load scenarios. This could be due to unmodeled losses, such as switching losses in the ESC and eddy current losses in the motor [10]. Therefore, the samples in the nonlinear least square problem was chosen to be weighed with $I_a^2$, which yields overall more accurate current and speed predictions.

Table II shows the resulting parameters for the voltage and torque balances. The $k_E$ value of 0.0134 corresponds to a $k_V$ of 712.6, which is close to the specified value of 610 rpm/V. Also, the internal resistance is of the same order of magnitude as the value provided in the technical data sheet of the motor, which is 0.031 ohms. It should be mentioned that the speed controller and cables add to the total resistance. Note that it is here assumed that the $R$ and $k_E$ are constant. In practice this might not be the case due to e.g. temperature variations. However, if measurements of current and voltage are available, it is possible to continuously monitor these

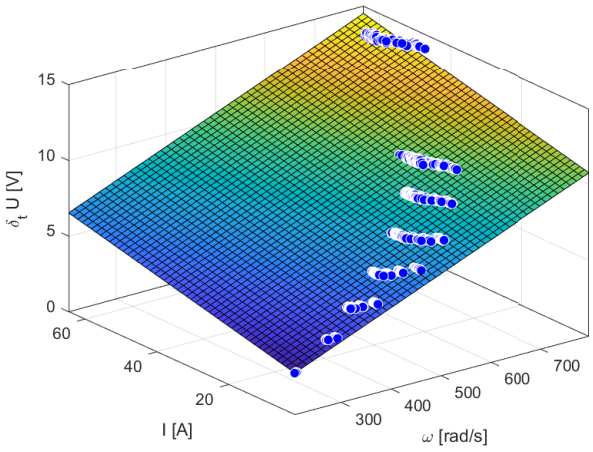


Fig. 6. Voltage balance fit.

coefficients with a suitable online estimation method using (5).

Figures 6 and 7 visualize the result of the fitting process, while the propeller speed predictions compared to the measured values are showed in Figure 8. Note the discrepancy during windmilling, with increasing errors at low throttle as airspeed increases. This is present due to leaving out windmilling data during identification. The reason for doing this is to improve estimates of electrical parameters as well as enabling reasonable current prediction, despite limitations of the electromechanical modeling in this domain. Figure 9 shows quite accurate propeller speed predictions for $V_a \approx 10.5$ m/s, while Figure 10 illustrates how the discrepancy increases in the low throttle region, although the predictions remain quite good for higher speed. Thrust predictions based on the predicted propeller speed will be presented and compared to the other thrust models in section V-D.

In Figure 11, which compares predicted and measured current, the predicted current is negative, but small, in the zero thrust regions. The root-mean-square error (RMSE) is $5.45$ A, which corresponds to $8.45\%$ of the maximum current of $64.5$ amperes. Figure 12 shows a zoomed in view for $V_a \approx 18.5$ m/s. The model overpredicts current in the medium load regions, and underpredicts in the high load region. This indicates that getting accurate results across the entire range of throttle settings might be difficult with a simple electromechanical model like this. Achieving a greater accuracy in a smaller range of throttle values should be possible by focusing on a subset of the data.

### B. Thrust Coefficient

Table III shows resulting thrust coefficients which have been identified from (21), while Figure 13 shows the thrust coefficient as a function of advance ratio. It is evident that a linear thrust coefficient fits the tested propeller well, at least in the range of advance ratios recorded in these experiments. The measured values show some variance that is increasing with higher advance ratio. This is mainly due to vibrations

TABLE II
PHYSICAL MODEL PARAMETERS; VOLTAGE AND TORQUE BALANCE FITS

| Parameters | | | | RMSE | $R^2$ |
|---|---|---|---|---|---|
| $R = 0.0587\ \Omega$ | $k_E = 0.0134$ Vs | | | 14.49 W | 0.9971 |
| $C_{Q,0} = 0.0078$ | $C_{Q,1} = -0.0058$ | $i_0 = 1.97$ A | $c_v = 0$ Nm·s | 0.0934 Nm | 0.9792 |

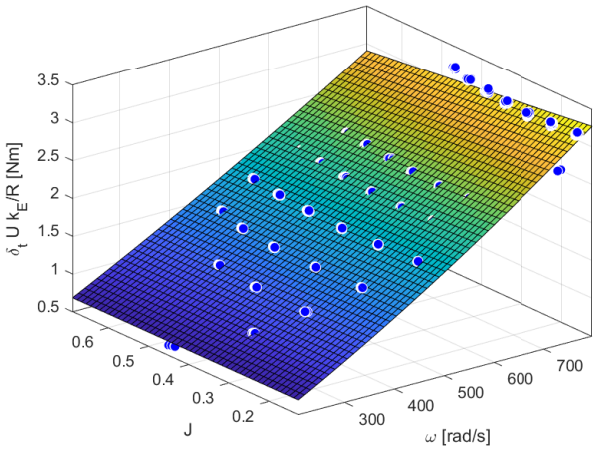


Fig. 7. Torque balance fit.

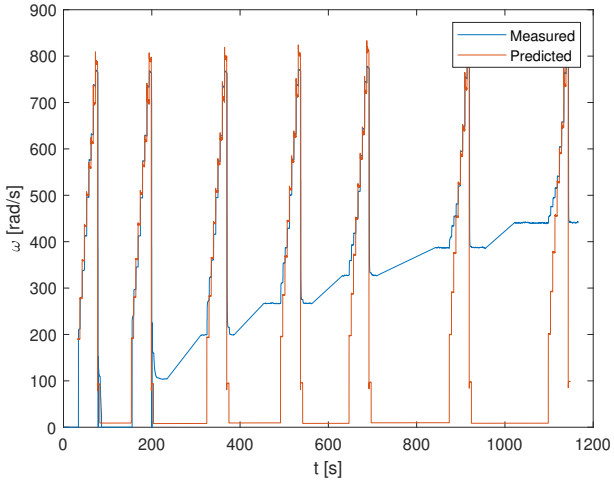


Fig. 8. Propeller speed prediction.

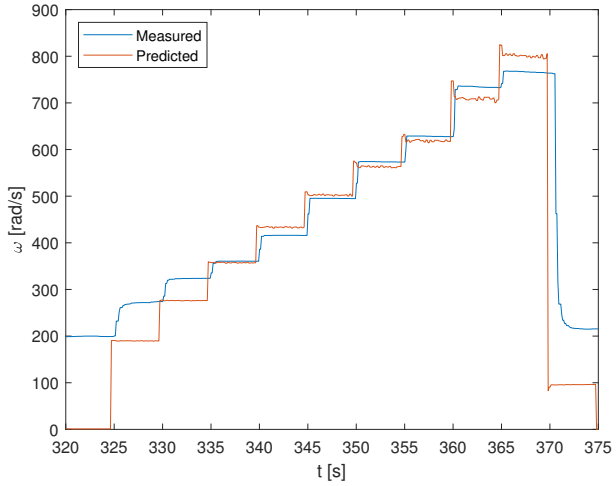


Fig. 9. Propeller speed for $V_a \approx 10.5$ m/s.

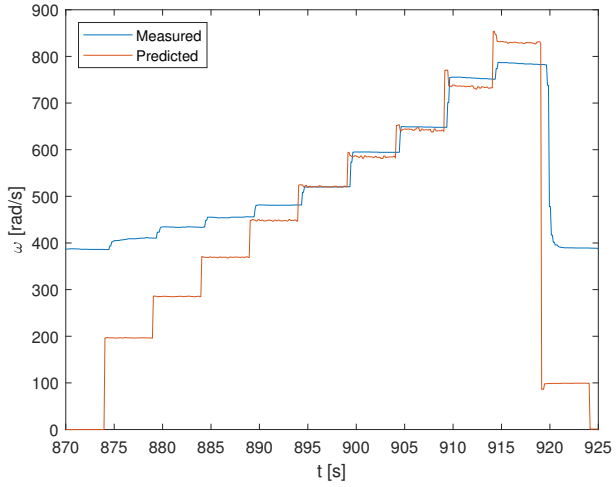


Fig. 10. Propeller speed for $V_a \approx 18.5$ m/s.

within the wind tunnel which increase with the fan speed of the wind tunnel. This is also seen in the coefficient of determination, $R^2$, value in Table III, where an $R^2$ number close to 1.0 indicates that all the variance of the residuals is explained by the variance of the data.

Figure 14 shows thrust predictions using the thrust coefficient calculated using measurements of propeller speed. The predicted thrust follows the measured thrust force closely. In Figure 15, for each series of steps, the airspeed is increasing with time. The predicted thrust clearly takes into account that the thrust decreases with increasing airspeed.

### C. Beard & McLain and Fitzpatrick Models

Table IV shows resulting coefficients for the Beard & McLain and Fitzpatrick models. RMSE and $R^2$ values indicate that the Fitzpatrick model fits the experimental data better than the simpler Beard & McLain model, and that the model fits the data quite good with an $R^2$ value of 0.94. Comparing Figure 16 with Figure 17 shows that the Fitzpatrick model better represents the nonlinear airspeed dependence by ”twisting” the fitted surface. As seen in Figure 18, a downside to the simplicity of the Beard & McLain model is that for higher airspeeds, the predicted thrust becomes negative for low throttle values, which is also easily seen from Equation (22).

TABLE III
THRUST COEFFICIENT PARAMETERS

| Coefficients | | RMSE | $R^2$ |
|---|---|---|---|
| $C_{T,0} = 0.126$ | $C_{T,1} = -0.1378$ | 0.0045 | 0.9997 |

TABLE IV
B&M AND FITZPATRICK MODEL COEFFICIENTS

| Model | Coefficients | RMSE | $R^2$ |
|---|---|---|---|
| Beard & McLain | $\eta_p = 0.178$, $k_m = 54.84$ m/s, | 3.43 N | 0.83 |
| Fitzpatrick | $\eta_p = 0.248$, $k_m = 37.42$ m/s, | 2.09 N | 0.94 |

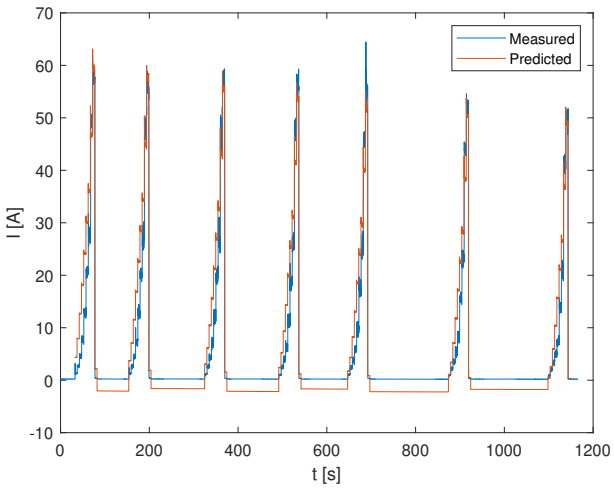


Fig. 11. Current prediction.

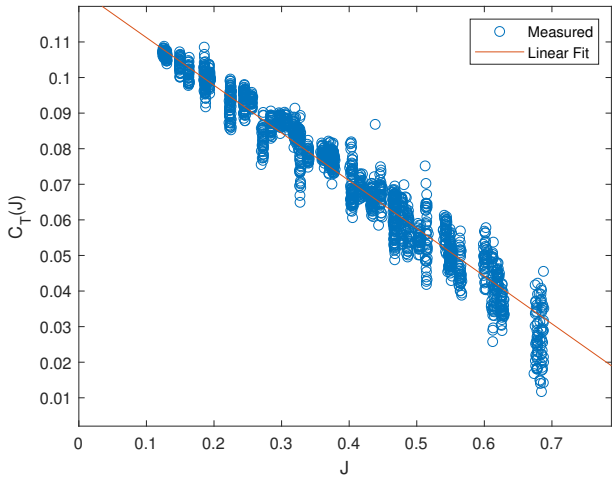


Fig. 13. Thrust coefficient as a function of advance ratio.

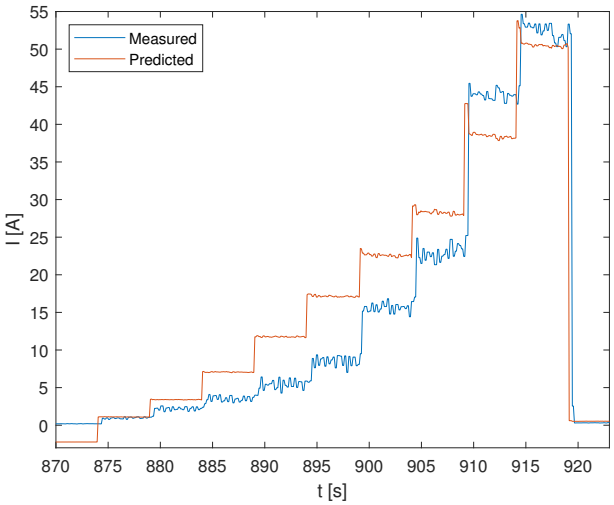


Fig. 12. Current prediction, zoomed in view, $V_a \approx 18.5$ m/s.

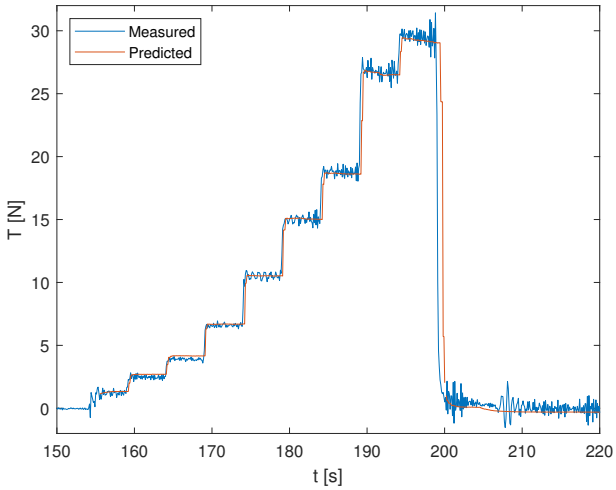


Fig. 14. Thrust prediction using $\omega$ and $C_T$.

### D. Comparison of Thrust Models

Figures 19 and 20 show a comparison of thrust predictions for the different models. Results are presented for two different airspeeds, $V_a \approx 10.5$ and $V_a \approx 18.5$ m/s. The graphs labeled "RPM Meas." are calculated using thrust coefficients and RPM measurements, while the graphs labeled "No RPM Meas." are based on propeller speed predictions using the physical model.

For both airspeeds, the thrust predictions using RPM measurements are clearly most accurate. Looking at the other three, the physical and Beard & McLain models predict negative thrust in the low throttle regions (especially at the higher airspeed). An advantage of the Fitzpatrick model is that it does not predict negative thrust, at least for the range of airspeeds seen in this experiment. The fact that the Beard & McLain model predicts negative thrust at higher airspeeds has already been pointed out. Low throttle and

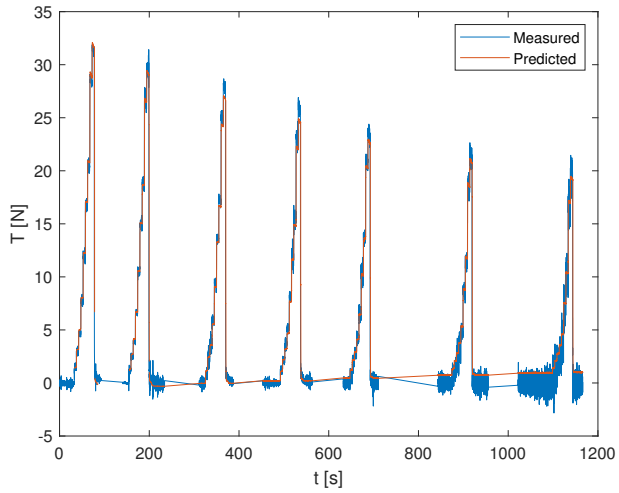


Fig. 15. Thrust prediction using $\omega$ and $C_T$.

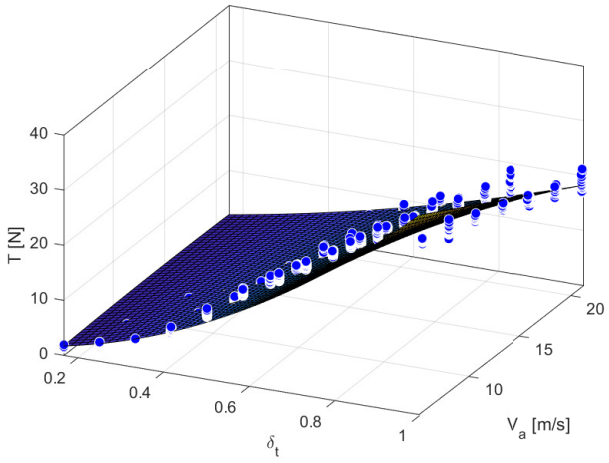


Fig. 17. Fitzpatrick model.

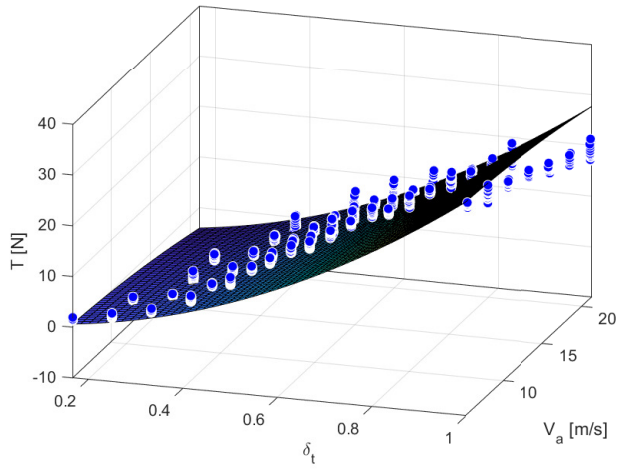


Fig. 16. Beard & McLain model.

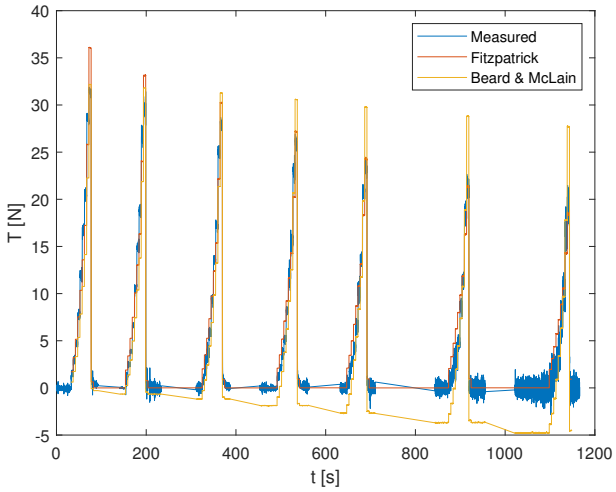


Fig. 18. Comparison of approximate models.

higher airspeeds gives high advance ratios. This behaviour of the physical model is most likely tied to the linear (in advance ratio) approximation of the thrust coefficient as well as the underprediction of propeller speed due to windmilling. Overall, except at the highest thrust setting, the physical model seem to be the most accurate of the three for thrust values above approximately 3 Newtons. The overprediction of thrust of the physical model in the highest thrust region can be tied to the overprediction of propeller speed seen in Figures 9 and 10. Table V shows a comparison of root-mean-square and max errors between the four models. With regards to both RMS and max errors, the best result is obtained using RPM measurements, with an RMSE of only 2.2 percent of maximum thrust and a max error of 9.1 percent. Comparing the other three, the accuracy of the physical model using predicted RPM is the best, slightly better than the Fitzpatrick model.

TABLE V
THRUST PREDICTION ERRORS (PERCENTAGE OF MAX THRUST SHOWN IN PARENTHESES)

| Model | RMSE | | Max Error | |
|---|---|---|---|---|
| Beard & McLain | 3.43 N | (10.76%) | 10.54 N | (33.06%) |
| Fitzpatrick | 2.09 N | (6.56%) | 5.52 N | (17.32%) |
| Predicted RPM | 1.44 N | (4.52%) | 4.80 N | (15.06%) |
| Measured RPM | 0.70 N | (2.20%) | 2.90 N | (9.10%) |

## VI. CONCLUSION

This work presents a multiphysical model of an electric propulsion system of a small UAV and compares it to two approximate models found in the literature. Experimental results show that the proposed model is able to make accurate predictions of forward thrust, as well as estimates of demanded battery current and propeller speed using only the battery voltage, throttle and the airspeed as inputs. The thrust predictions prove to be more accurate than the predictions made by the approximate models although with the drawback of a higher number of parameters which need to be identified.

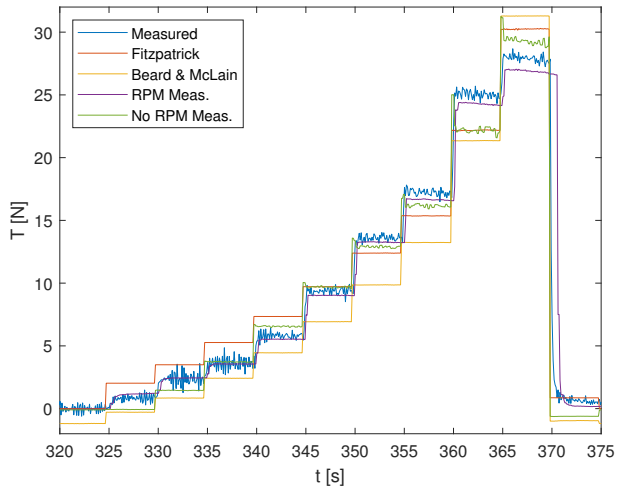


Fig. 19. Thrust prediction comparison for $V_a \approx 10.5$ m/s.

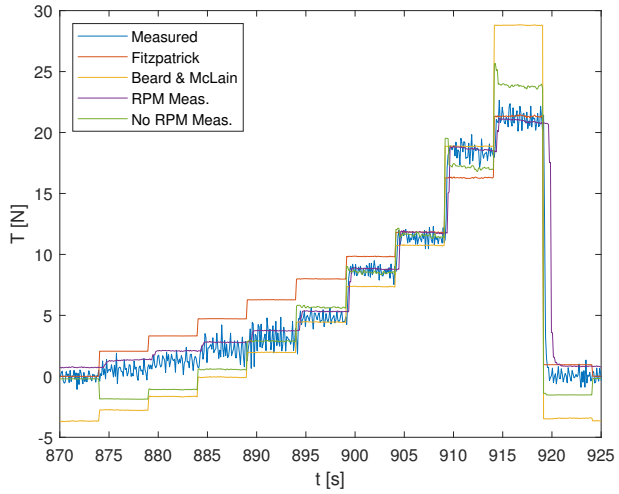


Fig. 20. Thrust prediction comparison for $V_a \approx 18.5$ m/s.

The identified model can be used for in-flight fault detection and aerodynamic drag estimation. When combined with a model of the power source [19], it can also be used for range prediction as well as for finding an optimal operating point for the aircraft.

## Acknowledgments

The authors would like to thank Professor Jason Hearst for access to the wind tunnel and his assistance during the experiments. This research was funded by the Research Council of Norway through the Centres of Excellence funding scheme, grant number 223254 - NTNU AMOS, and grants 282004 and 261791.

## References

[1] Brushless DC (BLDC) Motor Fundamentals Application Note. AN885. Technical report, Microchip, AZ, USA, 2003.

[2] Randal W Beard. Uavbook Supplement. Additional thoughts on propeller thrust model. Technical report, 2014.

[3] Randal W. Beard and Timothy W. McLain. *Small Unmanned Aircraft: Theory and Practice*. Princeton University Press, 2012.

[4] Randal W. Beard and Timothy W. McLain. Small Unmanned Aircraft - Supplement. Technical report, Princeton University Press, 2019.

[5] A. Betz and L. Prandtl. Schraubenpropeller mit geringstem Energieverlust. *Nachrichten von der Gesellschaft der Wissenschaften zu Göttingen, Mathematisch-Physikalische Klasse*, 2, 1919.

[6] Thomas F. Coleman and Yuying Li. On the convergence of interior-reflective Newton methods for nonlinear minimization subject to bounds. *Mathematical Programming*, 67(2):189224, 1994.

[7] Thomas F. Coleman and Yuying Li. An Interior Trust Region Approach for Nonlinear Minimization Subject to Bounds. *SIAM Journal on Optimization*, 6(2):418–445, 2005.

[8] P Fitzpatrick. Calculation oft Thrust in a Ducted Fan Assembly for Hovercraft. Technical report, Hovercraft Club of Great Britain, 2003.

[9] R E Froude. On the part played in propulsion by differences of fluid pressure. *Trans. Inst. Nav. Arch.*, 30:390, 1889.

[10] Darren Lance Gabriel, Johan Meyer, and Francois Du Plessis. Brushless DC motor characterisation and selection for a fixed wing UAV. *IEEE AFRICON Conference*, 2011.

[11] Waqas Khan and Meyer Nahon. Toward an accurate physics-based UAV thruster model. *IEEE/ASME Transactions on Mechatronics*, 18(4):1269–1279, 2013.

[12] Jeremy Lesprier, Jean Marc Biannic, and Clement Roos. Modeling and robust nonlinear control of a fixed-wing UAV. *2015 IEEE Conference on Control and Applications, CCA 2015*, pages 1334–1339, 2015.

[13] Cunjia Liu and Wen-Hua Chen. Disturbance Rejection Flight Control for Small Fixed-Wing Unmanned Aerial Vehicles. *Journal of Guidance, Control, and Dynamics*, 39(12):2810–2819, 2016.

[14] Barnes W. McCormick. *Aerodynamics, Aeronautics and Flight Mechanics*. Wiley, second edition, 1995.

[15] Olaf Moseler and Rolf Isermann. Application of model-based fault detection to a brushless DC motor. *IEEE Transactions on Industrial Electronics*, 47(5):1015–1020, 2000.

[16] José Pinto, Pedro Calado, José Braga, Paulo Dias, Ricardo Martins, Eduardo Marques, and JB Sousa. Implementation of a control architecture for networked vehicle systems. *IFAC Proceedings Volumes*, 45(5):100–105, 2012.

[17] Libor Prokop and Leos Chalupa. 3-Phase BLDC Motor Control with Sensorless Back EMF Zero Crossing Detection Using 56F80x. Technical report, Freescale Semiconductor, 2005.

[18] W.J.M. Rankine. On the mechanical principles of the action of propellers. *6th session of the Institution of Naval Architects*, (9):13–19, 1865.

[19] Bhaskar Saha, Edwin Koshimoto, Cuong C. Quach, Edward F. Hogge, Thomas H. Strom, Boyd L. Hill, Sixto L. Vazquez, and Kai Goebel. Battery health management system for electric UAVs. *IEEE Aerosp. Conf. Proc.*, pages 1–9, 2011.

[20] Michael S Selig. Modeling Propeller Aerodynamics and Slipstream Effects on Small UAVs in Realtime. In *AIAA Atmospheric Flight Mechanics*, Toronto, Canada, 2010.

[21] Robert F. Stengel. Exploring the Flight Envelope. In *Flight Dynamics*, pages 29–146. Princeton University Press, 2004.